3. B. Yaakobi, R. L. McCrory, S. Skupsky, J. A. Delettrez, P. Bourke, H. Deckman, C. F. Hooper, and J. M. Soures, Opt. Commun. **34**, 213 (1980).

4. LLE Review **22**, 51 (1985).

5. R. Epstein, Phys. Rev. A **43**, 961 (1991).

6. R. Epstein and B. Yaakobi, Phys. Rev. A **44**, 5111 (1991).

7. C. F. Hooper, Jr., D. P. Kilcrease, R. C. Mancini, L. A. Woltz, D. K. Bradley, P. A. Jaanimagi, and M. C. Richardson, Phys. Rev. Lett. **63**, 267 (1989).

8. L. L. House, Astrophys. J. Suppl. Ser. 155 **18**, 21 (1969).

9. T. A. Carlson *et al.*, Atomic Data **2**, 63 (1970).

1.B Nonlocal Heat-Transport Effects on the Filamentation of Light in Plasmas

Laser filamentation is potentially a serious problem for future inertial-confinement-fusion (ICF) schemes that produce long-scale-length plasmas.[1] The filamentation process occurs as a result of spatial variations in the incident laser irradiation on target that form self-focusing density channels along the direction of propagation. The instability is referred to as ponderomotive[2] or thermal,[3] depending on whether the density channels are created primarily by ponderomotive or thermal forces. Some undesirable consequences of filamentation are the triggering of parametric instabilities and the production of nonuniform ablation pressures in direct-drive ICF.

A recent kinetic analysis of filamentation has shown that the thermal mechanism dominates over the ponderomotive mechanism for most cases of interest to ICF.[4] This result comes from a reduction in the electron thermal conductivity for temperature variations over distances shorter than about 200 λ_e, where

$$\lambda_e = T^2 / \left[4\pi n e^4 (Z+1)^{1/2} \ln\Lambda \right]$$

is the delocalization length, or mean free path, of a thermal electron (T is the electron temperature, n is the electron number density, e is the magnitude of the electron charge, Z is the ionization number, and $\ln\Lambda$ is the Coulomb logarithm). A reduced thermal conductivity results in larger temperature modulations, driving larger density modulations and enhancing the instability. This analysis has since been confirmed by 2-D Fokker-Planck (FP) simulations, using the SPARK code,[5] which also reproduce well the filamentation experiments performed by Young *et al.* (1988).[6] Successful comparisons between SPARK simulations and experiments also provide indirect evidence of flux inhibition in a laser-fusion plasma corona.

The aim of this article is to (a) improve our understanding of nonlocal heat transport and check the accuracy of the reduced form of the FP equation used in our analysis, (b) review and improve the kinetic theory of laser filamentation, (c) provide a comparison between 2-D SPARK simulations and recent filamentation experiments by Young (1991),[7] and (d) discuss the implications of laser filamentation for the design of future ICF targets. The main conclusions are then presented.

Nonlocal Heat Transport

It is well known that for strong temperature gradients, such as are found in ICF plasmas, the electron heat flow can become inhibited when compared with the classical value[8] $\mathbf{q}_{SH} = -\kappa_{SH}\nabla T$ [where κ_{SH} is the classical Spitzer-Härm[9] (SH) heat conductivity]. One popular solution to this problem has been to limit the SH heat flow to some fraction f of the "free-streaming" heat flow $q_f = nm\upsilon_t^3$ (where m is the electron mass and $\upsilon_t = \sqrt{T/m}$), by setting $\mathbf{q} = \mathbf{q}_{SH} / \left(1 + |\mathbf{q}_{SH}|fq_f\right)$.[10]

A more subtle, yet important, heat-flow reduction effect has been shown to arise even for arbitrarily small levels of heat flow $\left(\text{i.e., } |\mathbf{q}_{SH}| \ll fq_f\right)$,[11] provided the corresponding spatial temperature-modulation wavelength $\lambda_\perp$ is less than about $200\,\lambda_e$.[4,12] The appropriate reduction in the heat conductivity has been recently calculated for the case where a spatially modulated inverse-bremsstrahlung heating source is balanced by heat conduction in a homogeneous plasma with fixed ions.[4] More specifically, SPARK has been used to calculate the effective heat conductivity κ, defined by the the energy balance equation $k_\perp^2 \kappa \delta T = \delta S$, where $k_\perp \left(= 2\pi / \lambda_\perp\right)$ is the modulation wave number, and δT and δS are the amplitudes of the temperature and heat source modulations, respectively. The result of the calculations are shown in Fig. 49.9, where we plot κ/κ_{SH} as a function of $k_\perp\lambda_e$. As expected, in the collisional limit $\left(k_\perp\lambda_e \to 0\right)$ $\kappa \to \kappa_{SH}$.

The strong reduction in conductivity when $k_\perp\lambda_e \gtrsim 0.03$ is because there are two main groups of electrons: a thermal group, which is representative of the plasma temperature, where most of the collisional heating (caused by inverse bremsstrahlung) is absorbed; and a suprathermal group, with velocities close to $3.7\,\upsilon_t$, which is responsible for carrying most of the heat flow.[8] In fluid theory, these two groups are assumed to be coupled by a single Maxwellian electron distribution in velocity. However, in practice, if the characteristic mean free path of the heat-carrying group is longer than the relevant spatial scale length ($\lambda_\perp$ in our case), these electrons will become decoupled from their thermal counterpart and establish a uniform distribution in configuration space. The reduction in the spatial gradient of the electrons at $3.7\,\upsilon_t$ will then lead to a reduction in the effective heat conductivity. Since the mean free path of an electron is proportional to υ^4 it is not surprising that this nonlocal transport effect becomes important for $\lambda_\perp \lesssim 200\,\lambda_e$ (instead of $\lambda_\perp \lesssim \lambda_e$, where λ_e is defined for a thermal electron).

In order to obtain more insight into the heat-flow process, let us first consider the Legendre expansion of the electron distribution function in one dimension

Fig. 49.9

Ratio of the effective conductivity κ to the Spitzer-Härm conductivity κ_{SH} as a function of $k_\perp \lambda_e$, where $k_\perp$ is the perturbation wave number and λ_e is the delocalization length. Solid circles correspond to SPARK results [in the (f_0, f_1) approximation], and the solid curve is a numerical fit to that data. The effect of using higher-order Legendre modes in SPARK is shown by the open circles.
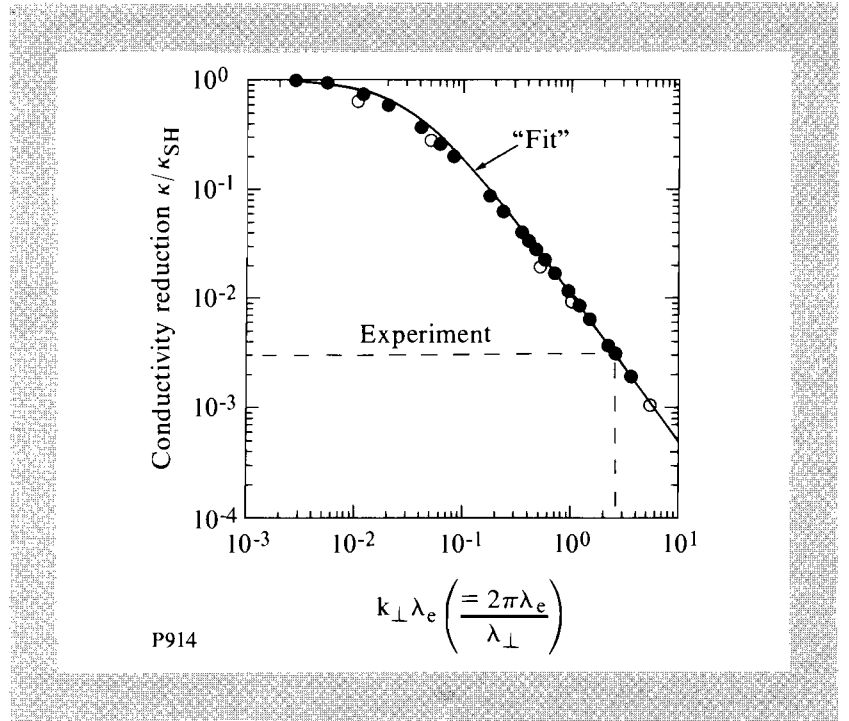
$$f(x, \mathbf{v}, t) = f_0(x, \mathbf{v}, t) + \mu f_1(x, \mathbf{v}, t) + \ldots, \qquad (1)$$

where μ is the direction cosine. We now define the electron heat flow in the x direction as follows:

$$q(x) = \frac{2\pi m}{3} \int_0^\infty d\mathbf{v}\, \mathbf{v}^5 f_1(x, \mathbf{v}). \qquad (2)$$

In fluid theory, an expression for f_1 can be obtained by assuming small departures from the Maxwellian distribution function f_M and truncating the expansion in Eq. (1) after f_1 (e.g., Ref. 9), i.e.,

$$f_1^{SH}(x, \mathbf{v}) = \lambda_s(\mathbf{v}) \left(\frac{\mathbf{v}^2}{2\mathbf{v}_t^2} - 4 \right) \frac{1}{T} \frac{\partial T}{\partial x} f_0(x, \mathbf{v}), \qquad (3)$$

where

$$f_0 = f_M, \lambda_s(\mathbf{v}) = \mathbf{v}^4 \left/ \left[4\pi n \left(e^2 / m \right)^2 (Z+1) \ln \Lambda \right] \right.$$

is the 90° angular scattering mean free path. [For simplicity, Eq. (3) is given in the high-Z limit.] Substituting Eq. (3) into Eq. (2) yields q_{SH}, and hence κ_{SH}. However, as indicated earlier, nonlocal transport effects can lead to departures from a Maxwellian that invalidate the use of Eq. (3). Using the FP code SPARK, we have calculated the self-consistent f_0 that leads to the modified heat flow. In particular, we have calculated the integrand of the general heat-flow formula [Eq. (2)], i.e., $Q(\mathbf{v}) = \mathbf{v}^5 f_1$. This has been done for the model heat-flow problem of Fig. 49.9.

Figure 49.10 plots $Q(\upsilon)$ as a function υ/υ_t, for three levels of collisionality: (a) $k_\perp \lambda_e = 0.01$; (b) $k_\perp \lambda_e = 0.05$; and (c) $k_\perp \lambda_e = 0.2$. The dashed curve (which is normalized to unity) is based on $f_1{}^{SH}$, using the calculated temperature from the FP code. Since the areas under the curves are proportional to the respective levels of the heat flow, curves (a)–(c) illustrate the effective reduction in the level of heat flow, relative to q_{SH}, as $k_\perp \lambda_e$ increases. These correspond to the values of κ/κ_{SH} in Fig. 49.9.
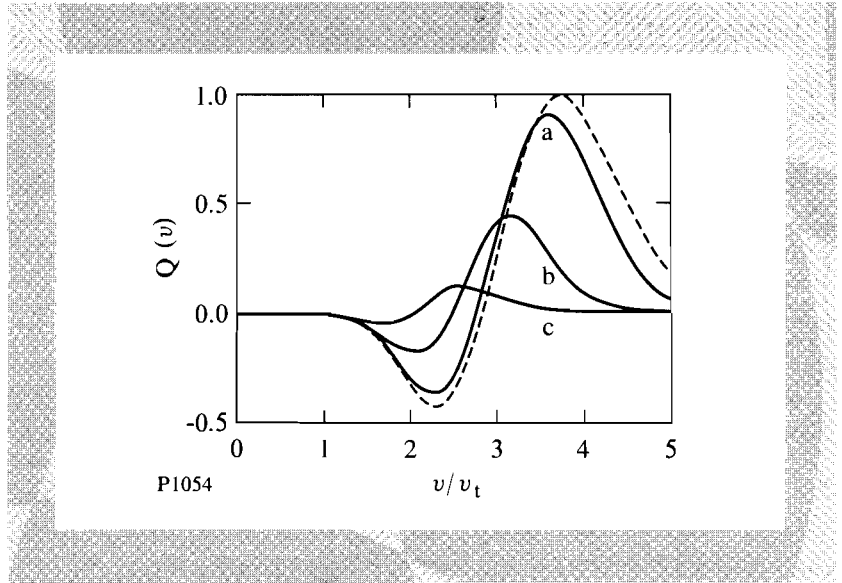
Fig. 49.10
Plot of the heat flux $Q(\upsilon)$, normalized to the corresponding maximum value of $Q_{SH}(\upsilon)$, as a function of υ/υ_t. The dashed curve is the result based on Spitzer-Härm heat flow and the solid curves are obtained from Fokker-Planck simulations for: (a) $k_\perp \lambda_e = 0.01$, (b) $k_\perp \lambda_e = 0.05$, and (c) $k_\perp \lambda_e = 0.2$.

P1054

Another important feature of the FP curves is that as the collisionality decreases, i.e., as $k_\perp \lambda_e$ increases, the characteristic velocity υ^* of the main heat-carrying electrons is reduced. Indeed, for $k_\perp \lambda_e = 0.2$ (curve c) $\upsilon^* \approx 2.6\,\upsilon_t$, whereas for the classical collisional case $\upsilon^* \approx 3.7\,\upsilon_t$. So the reduction in the effectiveness of heat flow at short perturbation wavelengths is because the heat is carried mainly by lower velocity electrons, which have higher collision rates.

There are two main approximations in the kinetic treatment of the heat flow adopted in this section. They are the Lorentz approximation (or high-Z) of the collision operator, and the truncation of the Legendre polynomial expansion of the distribution function [i.e., Eq. (1)] after the first two terms.

The first approximation can be partially corrected for by introducing a Z-dependent factor in the angular scattering mean free path λ_s that yields the exact heat-flow coefficient in the strong collisional limit (see Ref. 5). This has some minor implications for the linear theory of filamentation as discussed in the next section.

The second approximation can also be corrected for by appropriately modifying λ_s. To do this we first substitute Eq. (1) into the time-independent electron FP equation (in the Lorentz approximation) and linearize the resultant coupled equations[13] with a harmonic perturbation of the form

$f_0(x, \upsilon) = f_M(\upsilon) + \delta f_0(\upsilon) \exp(ik_\perp x)$, and $f_1(x, \upsilon) = f_1(\upsilon) \exp(ik_\perp x)$, where $l \geq 1$ refers to the Legendre mode, i.e.,

$$\frac{ik_\perp \upsilon}{3} f_1 = C_{ee}(f_M, \delta f_0) + \delta S_{ib}, \tag{4}$$

$$ik_\perp \upsilon \delta f_0 - \frac{e\delta E}{m} \frac{\partial f_M}{\partial \upsilon} + \frac{2}{5} ik_\perp \upsilon f_2 = -\frac{\upsilon}{\lambda_s} f_1, \tag{5}$$

$$\vdots$$

$$\frac{l}{2l-1}(ik_\perp \upsilon f_{l-1}) + \frac{l+1}{2l+3}(ik_\perp \upsilon f_{l+1}) = -\frac{l(l+1)}{2} \frac{\upsilon}{\lambda_s} f_l. \tag{6}$$

Here, δE is the perturbed electric field, C_{ee} is the electron thermalization operator and δS_{ib} is the inverse-bremsstrahlung heating operator.[14] The electron-ion energy exchange is neglected in Eq. (4) since $m \ll m_i$. After straightforward substitution of Eq. (6) into Eq. (5), it can be shown that the contribution of f_2, f_3, ... into f_1 can be accounted for by defining a new scattering mean free path λ_s^* as follows:

$$\lambda_s^* = \lambda_s \left(1 + \frac{c_2 k_\perp^2 \lambda_s^2}{1 + \dfrac{c_3 k_\perp^2 \lambda_s^2}{1 + \cdots}} \right)^{-1} \tag{7}$$

where

$$c_l = \frac{4}{(4l^2 - 1)(l^2 - 1)}. \tag{8}$$

Such a correction has been introduced into the FP code SPARK and the calculations shown in Fig. 49.9 have been repeated. The new results, displayed as open circles in Fig. 49.9, fall within 10% of the original results. Thus, for the linearized heat-flow problem considered here, it is justifiable to truncate the Legendre polynomial expansion after the first two terms. This conclusion also appears to hold for a variety of heat-flow problems.[11,15]

Analytic Model

The kinetic theory of laser filamentation has been developed in Ref. 4. Here, we review the model and present some improvements with regard to the Z dependence.

The analysis follows the conventional approach of linearizing the electromagnetic wave equation using the slowly-varying-envelope approximation and assuming momentum and energy balance.[2,3] The formula for the spatial growth rate K of the average electric field along its direction of propagation is given by

$$K = \frac{k_\perp}{2\sqrt{\varepsilon}} \left(2\frac{n}{n_c} \left\{ \gamma_p + \gamma_T \left(\frac{\kappa_{SH}}{\kappa} \right) \frac{\omega^2}{k_\perp^2 c^2} \right\} - \frac{k_\perp^2 c^2}{\omega^2} \right)^{1/2} , \qquad (9)$$

where $k_\perp$ is the perturbation wave number perpendicular to the direction of propagation, c is the speed of light, ω is the laser frequency, n/n_c is the ratio of the electron number density to its critical density and $\varepsilon = (1 - n/n_c)$. Factors γ_p and γ_T, representing ponderomotive and thermal mechanisms, respectively, are defined by

$$\gamma_p = \frac{\text{ponderomotive pressure}}{\text{plasma thermal pressure}} = 9.33 \times 10^{-3} \frac{\lambda_{laser}^2 (\mu m) I(10^{14}\,W/cm^2)}{\sqrt{\varepsilon}(1 + 1/\langle Z \rangle) T(keV)} \quad (10)$$

and

$$\gamma_T = \frac{\text{inverse bremsstrahlung heating rate}}{\text{thermal conduction rate across } (c/\omega)} = 8.95 \times 10^{-9}$$

$$\frac{I(10^{14}\,W/cm^2)\left(Z^*\right)^2 (\ln \Lambda)^2}{T^5(keV)\phi\sqrt{\varepsilon}} \left(\frac{n}{n_c} \right)^2 , \qquad (11)$$

where λ_{laser} is the laser wavelength, T is the background electron temperature (assumed equal to the ion temperature), I is the incident laser intensity, $\langle Z \rangle$ is the average ionization number (where $\langle\ \rangle$ denotes an average over the ion species), $Z^* = \langle Z^2 \rangle / \langle Z \rangle$ and $\phi = (Z^* + 0.24)/(1 + 0.24\,Z^*)$. The ratio of the effective thermal conductivity to the classical SH conductivity has been numerically calculated using SPARK, and plotted in Fig. 49.9. An accurate fit to the results is given by

$$\frac{\kappa}{\kappa_{SH}} = \frac{1}{1 + (30 k_\perp \lambda_e)^{4/3}} , \qquad (12)$$

where the electron delocalization length is now defined by $\lambda_e = \eta\ T^2/[4\pi n e^4$ $(Z^* + 1)^{1/2} \ln \Lambda]$, which differs from an earlier definition (Ref. 4), by the factor

$$\eta = \left[\frac{\phi}{4.2} \frac{\left(Z^* + 1\right)}{Z^*} \right]^{1/2} \approx \left[\frac{0.24 + 1.24\left(Z^*\right) + \left(Z^*\right)^2}{4.2\left(Z^*\right) + \left(Z^*\right)^2} \right]^{1/2} \qquad (13)$$

This factor provides a correction at low Z (e.g., ionized CH has $Z^* = 5.3$; hence, $\eta = 0.83$) to account for the Lorentz approximation in the original SPARK simulations.

It is apparent from Eq. (9) that a reduction in the effective thermal conductivity relative to its classical value will enhance the thermal filamentation growth rate. Equation (12) shows that this occurs for a perturbation wavelength $\lambda_\perp$ less than some transition value defined by

$$\lambda_c = 60\pi\lambda_e = 3.21 \times 10^3 \frac{T^2(keV)\lambda_{laser}^2(\mu m)}{\ln\Lambda\left(Z^*/\phi\right)^{1/2}} \left(\frac{n_c}{n} \right) \mu m , \qquad (14)$$

such that when $\lambda_\perp = \lambda_c$, $\kappa/\kappa_{SH} = 1/2$.

From Eq. (9) it is straightforward to derive the optimum growth rates for thermal and ponderomotive filamentation. These are, respectively,

$$\left(K_{max}\right)_T^{FP} = 9.66 \times 10^{-3} \frac{(\ln \Lambda)^{1/2} Z^* I^{3/4} (10^{14}\, W/cm^2)}{\varepsilon^{7/8} T^{7/4} (keV) \phi^{1/4}} \left(\frac{n}{n_c}\right)^{5/4} \mu m^{-1} \quad (15)$$

and

$$\left(K_{max}\right)_p = 2.93 \times 10^{-2} \frac{\lambda_{laser} (\mu m) I(10^{14}\, W/cm^2)}{\varepsilon T (keV)(1 + 1/\langle Z \rangle)} \left(\frac{n}{n_c}\right) \mu m^{-1} \quad (16)$$

Comparison with the original formulas in Ref. 4 shows slight differences caused by improvements in the Z dependencies currently introduced. These differences are most important for low-Z multi-species plasmas, such as ionized CH, where one should differentiate between $\langle Z \rangle = 3.5$ and $Z^* = 5.3$.

SPARK Simulations

In this article SPARK is used as a 2-D Eulerian code, which solves the FP equation for the electrons, the ion fluid equations, and the paraxial wave equation for the laser light. Further details have been described in Refs. 16 and 5.

Here, we investigate the recent filamentation experiment reported by Young (1991),[7] where a 1.06-μm laser beam with a 100-ps FWHM pulse length was intentionally modulated in space and made to interact with a preformed underdense CH plasma. The resulting density perturbations, which are the signature of filamentation, were detected by means of a short-pulse (<100 ps) probe beam and were estimated to reach about 3%.

The conditions of the background plasma are assumed to be equivalent to those reported by Young et al. (1988) from a LASNEX simulation.[6] Following the same prescription used in Ref. 5 we consider a homogeneous temperature of 0.8 keV, and a uniform density in the x-y plane with a parabolic density profile in the z direction approximated by

$$\frac{n}{n_c} = 0.25 \left[1 - 0.6 \left(\frac{z}{400}\right)^2 \right], \quad (17)$$

where the density varies from 0.25 n_c at $z = 0$, to 0.1 n_c at $z = \pm 400$ μm. The interaction beam is modeled by $I(x, t) = I_0(t)(1 + 0.68 \cos k_\perp x)$, where $\lambda_\perp = 40$ μm, and $I(x = 0, t = 0) = 5 \times 10^{13}$ W/cm^2. The time dependence of $I_0(t)$ is modeled by a Gaussian with a 100-ps FWHM.

In view of the symmetry of the problem, the simulation is restricted to $0 \leq x \leq \lambda_\perp/2$, with reflective boundary conditions imposed at $x = 0$ and $\lambda_\perp/2$. Zero heat flow is likewise imposed at the $z = \pm 400$-μm boundaries, though free plasma flow is allowed there.

Figure 49.11 shows the surface plot of the normalized laser intensity I/I_0 in the x-z plane at the peak of the pulse (i.e., at $t = 0$ ps). (To illustrate the

periodicity of the problem the plots are extended to $1.5 \times \lambda_\perp$ along x.) The large intensity amplification observed in the FP simulation is principally caused by thermal self-focusing, whereas the small amount of amplification observed in the SH simulation is because of ponderomotive self-focusing only (the plasma is stable to classical thermal filamentation). The dominance of the so-called kinetic thermal mechanism over the ponderomotive one has been previously predicted by analytic theory[4] and by FP simulations under similar conditions,[5] and is a direct consequence of a reduction in heat conductivity, as discussed previously.

To compare with experiment it is more useful to calculate the density modulation $\delta n/n_0$, where n_0 is the average number density along x. Figure 49.12 plots $\delta n/n_0$, in terms of percentage values, for both FP and SH simulations at $t = 0$ ps. We observe from the figure that the density modulations predicted by the FP simulation are not only about ten times higher than those predicted by the SH simulation, but are also consistent with the 3% density-modulation value measured experimentally.

Implications to ICF

The simulation presented in the previous section serves to illustrate the physics of laser filamentation and provides a valuable comparison with experimental results. There are, however, important differences between these and the conditions relevant to ICF. In the first place, the plasma in ICF targets is not homogeneous, but has time-varying density gradients and flow. It has been shown, for example, that plasma flow perpendicular to the direction of laser propagation can either enhance or reduce the filamentation level, depending on whether it is subsonic or supersonic, respectively.[17] More important, however, is the fact that the laser irradiation can have a large spectrum of time-varying spatial modes.

Modern schemes for improving laser irradiation uniformity often involve some combination of phase plates,[18] which create a high-frequency speckle pattern in the target plane, and smoothing by spectral dispersion (SSD)[19] or induced spatial incoherence (ISI),[20] which introduce a temporal variation to the speckle pattern. The basic philosophy behind these schemes is that the high-frequency spatial modulation in the laser-energy deposition will be smoothed out by heat conduction in the plasma atmosphere. Further smoothing is then achieved, provided that the time variation in the speckle pattern is shorter than the characteristic hydrodynamic time scale of the plasma. Indeed, Schmitt has shown, by means of a 3-D filamentation code with linearized hydrodynamics and classical heat transport, that ISI or SSD can completely eliminate filamentation.[21] Unfortunately, the use of classical thermal conductivity in his simulations has led to an underestimate of the level of thermal filamentation.[22]

However, rather than perform filamentation simulations for specific types of laser irradiation profiles, we will restrict ourselves to the estimation of filamentation growth lengths L_g for some laser-target systems of current interest for direct-drive ICF, such as the 30-kJ OMEGA Upgrade system (currently under construction) and a hypothetical 5.9-MJ Laboratory Microfusion Facility (LMF). The plasma parameters are derived from hydrodynamic code simulations of CH spherical shells irradiated by 350-nm laser light.[23] They are
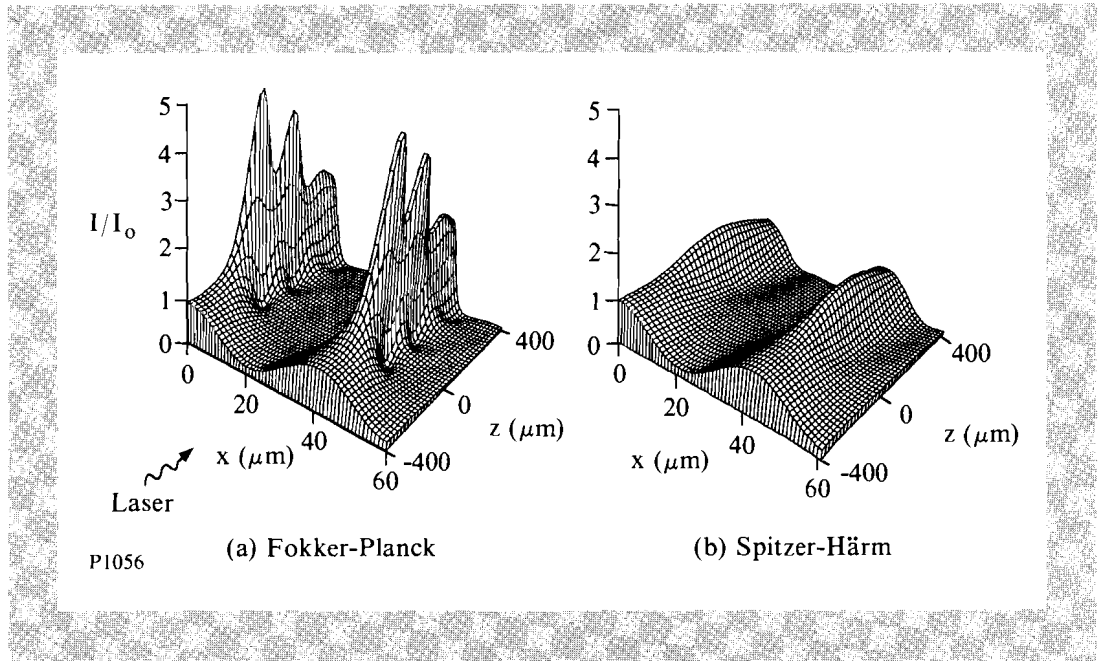
Fig. 49.11
Surface plots of the normalized laser intensity I/I_o on the x-z plane at $t = 0$ ps (i.e., at the peak of the laser pulse), for (a) Fokker-Planck transport and (b) Spitzer-Härm transport.
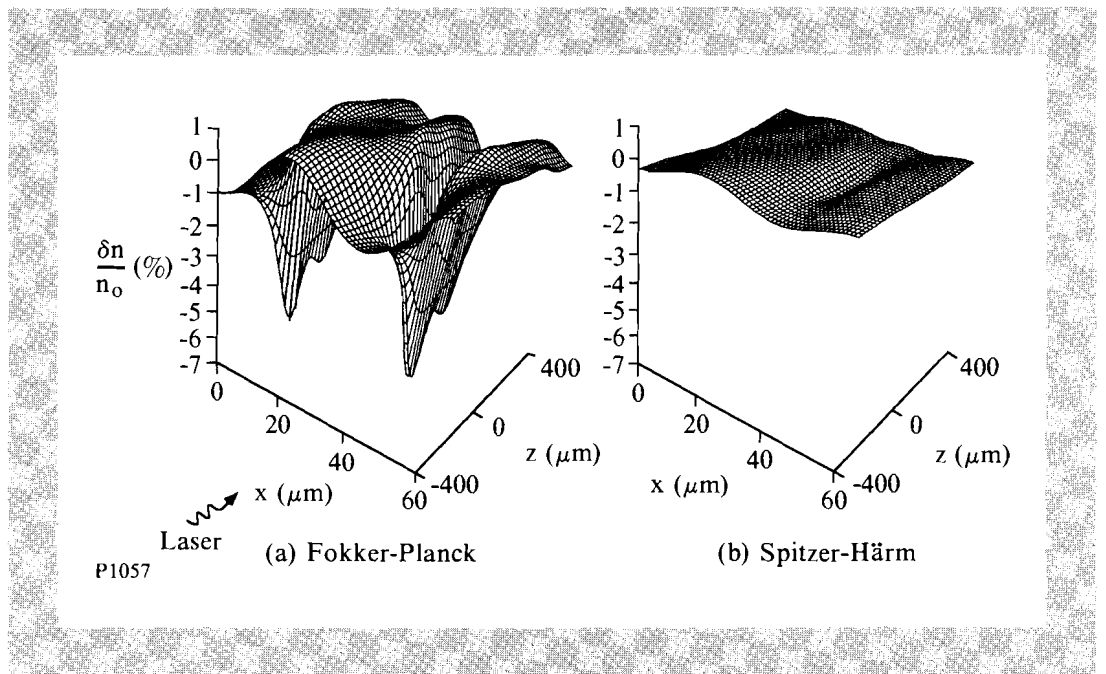

Fig. 49.12
Surface plots of normalized density modulation $\delta n/n_o$ on the x-z plane at $t = 0$ ps, for (a) Fokker-Planck transport and (b) Spitzer-Härm transport.

representative of plasma conditions at 0.1 n_c at peak laser intensity (quoted as a single-beam intensity).

The intensity filamentation growth length, which is related to the spatial growth rate by $L_g = (2K)^{-1}$, is calculated using Eq. (9) and plotted in Figs. 49.13 and 49.14 as a function of $\lambda_\perp$. The different solid curves correspond to the various filamentation mechanisms [i.e., kinetic thermal, ponderomotive and thermal (with $\kappa = \kappa_{SH}$)]. The horizontal lines indicate the density scale length L_n, and laser attenuation length L_{ib} (based on collisional absorption).

Fig. 49.13
Plot of the filamentation growth length (in microns) as a function of perturbation wavelength $\lambda_\perp$ (in microns) at the simulated plasma conditions expected for the OMEGA Upgrade [30 kJ, $\langle Z \rangle = 3.5$, $n/n_c = 0.1$, $T = 2.75$ keV, $I_o = 3.2 \times 10^{13}$ W/cm^2 (single beam), and $\lambda_L = 0.35$ μm] for three models of filamentation. If the growth length exceeds the plasma density scale length L_n (as is the case here for all models) the plasma is considered to be stable to filamentation.
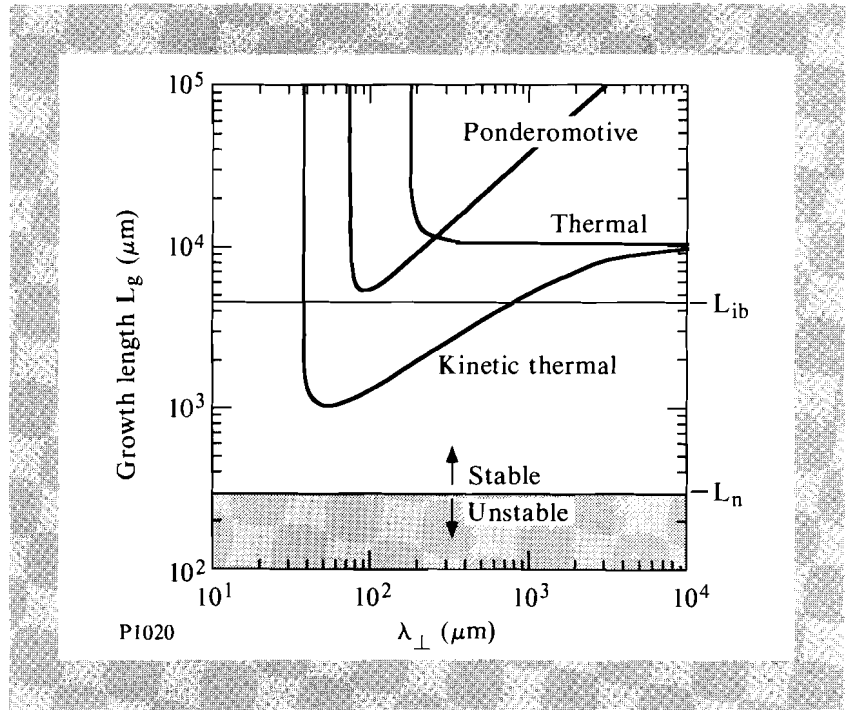
If we adopt the criterion for significant filamentation as $L_g <$ min (L_n, L_{ib}),[1] it is clear that (at least for the given plasma conditions) the proposed direct-drive ICF schemes appear not to be susceptible to filamentation. This filamentation criterion is based on linear homogeneous theory and, as such, does not take into account the possibility of stabilization through SSD or ISI schemes as previously discussed. Neither does it take into account the potential destabilizing effects of hot spots in the laser beam. Nevertheless, we believe that it provides a useful guideline for the likelihood of generating filaments.

In order to generalize our results to other plasma conditions we have also derived approximate formulas for the optimum growth lengths L_g, by simplifying Eqs. (15) and (16) (assuming $\ln \Lambda = 8$),

$$\left(L_g \right)_T^{FP} \approx 24 \, \frac{T^{1.8}(\text{keV})}{Z^* I^{0.8} (10^{14}\,\text{W}/\text{cm}^2) \left(\dfrac{n}{n_c} \right)^{1.3}} \, \mu\text{m}, \qquad (18)$$

and

$$\left(L_g\right)_P \approx 17 \frac{T(\text{keV})}{\lambda_{\text{laser}}(\mu\text{m})\, I(10^{14}\,\text{W}/\text{cm}^2)\left(\dfrac{n}{n_c}\right)}\mu\text{m}\ . \tag{19}$$
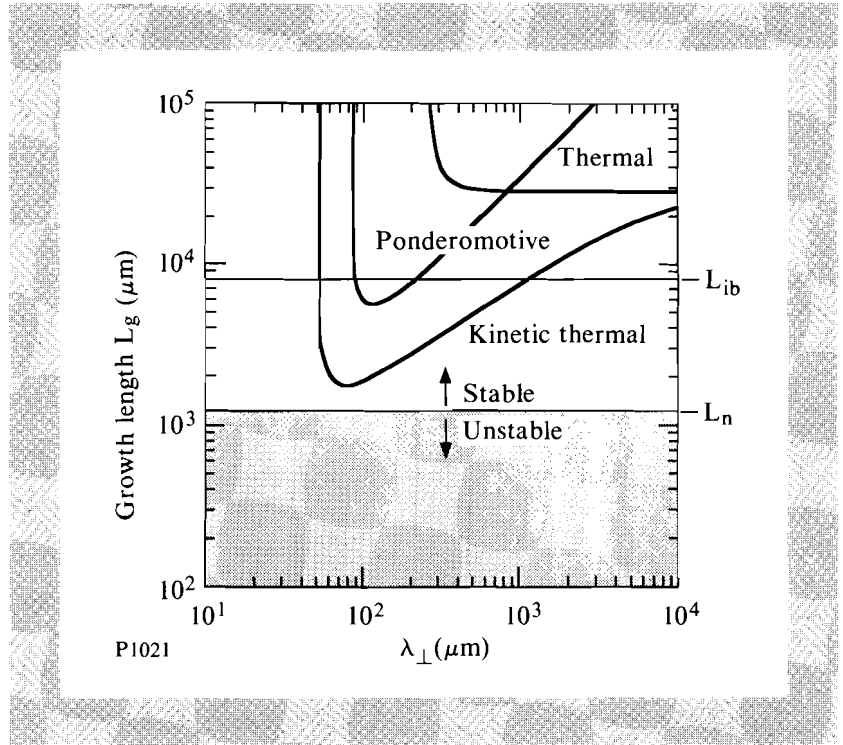
Fig. 49.14

Plot of the filamentation growth length (in microns) as a function of perturbation wavelength $\lambda_\perp$ (in microns) at the simulated plasma conditions expected for a direct-drive LMF system [5.9 MJ, $\langle Z \rangle = 3.5$, $n/n_c = 0.1$, $T = 4.5$ keV, $I_0 = 4.35 \times 10^{13}$ W/cm^2 (single beam), and $\lambda_L = 0.35\ \mu$m].

Conclusions

We have reviewed the nature of nonlocal heat transport and shown that plasmas with arbitrarily small temperature modulations of wavelength less than about 200 electron mean free paths can experience a significant reduction in the thermal conductivity as compared with classical Spitzer-Härm theory. The reduction in the effectiveness of the heat conduction has been demonstrated to be caused by a shift of heat-carrying electrons to lower velocities. Such nonlocal transport effects have been shown to be accurately modeled by expanding the electron distribution function into the first two Legendre modes only.

The effect of nonlocal electron heat transport on the linear stability theory of laser filamentation has been reviewed with some improvements for low-Z and multi-species plasmas. Simulations with the 2-D FP code SPARK reproduce well the density modulations observed in a filamentation experiment reported by Young. These results confirm the prediction of analytic theory that the main mechanism driving the filamentation of the laser is kinetic thermal rather than ponderomotive. Simple estimates of filamentation growth lengths, based on the linear homogeneous kinetic theory, have shown that for current direct-drive ICF systems, the single-beam intensities are below the threshold for filamentation.

ACKNOWLEDGMENT

REFERENCES

1. W. L. Kruer, Comments Plasma Phys. & Controlled Fusion **9**, 63 (1985); P. E. Young, Comments Plasma Phys. & Controlled Fusion **12**, 53 (1988); W. L. Kruer, Phys. Fluids B **3**, 2356 (1991); and W. Seka, Bull. Am. Phys. Soc. **36**, 2375 (1991).

2. P. Kaw, G. Schmidt, and T. Wilcox, Phys. Fluids **16**, 1522 (1973).

3. M. S. Sodha, A. K. Ghatak, and V. K. Tripathi, in *Progress in Optics*, edited by E. Wolf (North Holland, Amsterdam, 1976), Vol. 13, p. 169; J. N. McMullin, C. E. Capjack, and C. R. James, Comput. Phys. Commun. **23**, 31 (1981).

4. E. M. Epperlein, Phys. Rev. Lett. **65**, 2145 (1990).

5. E. M. Epperlein, Phys. Fluids B **3**, 3082 (1991).

6. P. E. Young *et al.*, Phys. Rev. Lett. **61**, 2336 (1988).

7. P. E. Young, Phys. Fluids B **3**, 2331 (1991).

8. D. R. Gray and J. D. Kilkenny, Plasma Phys. **22**, 81 (1980); A. R. Bell, R. G. Evans and D. J. Nicholas, Phys. Rev. Lett. **46**, 243 (1981); J. Delettrez, Can. J. Phys. **64**, 932 (1986) and references therein.

9. L. Spitzer, Jr. and R. Härm, Phys. Rev. **89**, 977 (1953).

10. R. C. Malone, R. L. McCrory, and R. L. Morse, Phys. Rev. Lett. **34**, 721 (1975).

11. A. R. Bell, Phys. Fluids **26**, 279 (1983).

12. E. M. Epperlein and R. W. Short, Phys. Fluids B **3**, 3092 (1991); E. M Epperlein, *Research Trends in Physics: Nonlinear and Relativistic Effects in Plasmas*, edited by V. Stefan (American Institute of Physics, New York, 1991) p. 43; LLE Review **42**, 57 (1990).

13. I. P. Shkarofsky, T. W. Johnston, and M. A. Bachynsky, *The Particle Kinetics of Plasmas* (Addison-Wesley, London, 1966); T. W. Johnston, J. Math. Phys. **7**, 1453 (1966).

14. A. B. Langdon, Phys. Rev. Lett. **44**, 575 (1980).

15. J. P. Matte and J. Virmont, Phys. Rev. Lett. **49**, 1936 (1982); J. P. Matte, T. W. Johnston, J. Delettrez, and R. L. McCrory, Phys. Rev. Lett. **53**, 1461 (1984); J. F. Luciani, P. Mora, and R. Pellat, Phys. Fluids **28**, 835 (1985).

16. E. M. Epperlein, G. J. Rickard, and A. R. Bell, Phys. Rev. Lett. **61**, 2453 (1988); E. M. Epperlein, G. J. Rickard, and A. R. Bell, Comput. Phys. Commun. **52**, 7 (1988); G. J. Rickard, A. R. Bell, and E. M. Epperlein, Phys. Rev. Lett. **62**, 2687 (1989).

17. R. W. Short, R. Bingham, and E. A. Williams, Phys. Fluids **25**, 2302 (1982).

18. Y. Kato *et al.*, Phys. Rev. Lett. **53**, 1057 (1984).

19. S. Skupsky, R. W. Short, T. Kessler, R. S. Craxton, S. Letzring, and J. M. Soures, J. Appl. Phys. **66**, 3456 (1989).

20. R. H. Lehmberg and S. P. Obenschain, Opt. Commun. **46**, 27 (1983).

21. A. J. Schmitt, Phys. Fluids B **3**, 186 (1990).

22. A. J. Schmitt, Bull. Am. Phys. Soc. **36**, 2335 (1991).

23. C. P. Verdon (private communication).